Celest Mech Dyn Astr (2010) 107:233–253
DOI 10.1007/s10569-010-9268-4

Periodic and quasi-periodic motions of a solar sail close to SL_1 in the Earth–Sun system

Ariadna Farrés · Àngel Jorba

Received: 1 November 2009 / Revised: 8 February 2010 / Accepted: 2 March 2010 /

Abstract Solar sails are a proposed form of spacecraft propulsion using large membrane mirrors to propel a satellite taking advantage of the solar radiation pressure. To model the dynamics of a solar sail we have considered the Earth–Sun Restricted Three Body Problem including the Solar radiation pressure (RTBPS). This model has a 2D surface of equilibrium points parametrised by the two angles that define the sail orientation. In this paper we study the non-linear dynamics close to an equilibrium point, with special interest in the bounded motion. We focus on the region of equilibria close to SL_1, a collinear equilibrium point that lies between the Earth and the Sun when the sail is perpendicular to the Sun–sail direction. For different fixed sail orientations we find families of planar, vertical and Halo-type orbits. We have also computed the centre manifold around different equilibria and used it to describe the quasi-periodic motion around them. We also show how the geometry of the phase space varies with the sail orientation. These kind of studies can be very useful for future mission applications.

Keywords Centre manifold · Graph transform · Invariant tori · Low–thrust · Artificially generated equilibrium points

1 Introduction

Solar Sails are a proposed form of spacecraft propulsion that takes advantage of the solar radiation pressure to propel a spacecraft by means of a large membrane mirror. The impact of the photons emitted by the Sun on the surface of the sail and its further reflection accelerates the spacecraft. Although the acceleration produced by the solar radiation pressure is

---

A. Farrés (✉) · À. Jorba
Departament de Matemàtica Aplicada i Anàlisi, Universitat de Barcelona,
Gran Via 585, 08007 Barcelona, Spain
e-mail: ari@maia.ub.es

À. Jorba
e-mail: angel@maia.ub.es

smaller than the one achieved by the traditional propulsion systems, this one is continuous and unlimited. This makes long term missions more accessible (McInnes 1999). It also opens a wide new range of possible mission applications that cannot be achieved by a traditional spacecraft, e.g. Geostorm Warning Mission, Polar Observer and the GeoSail (Macdonald and McInnes 2004).

The acceleration given by the sail depends on the orientation of the sail and its efficiency. In this paper we consider a flat and perfectly reflecting sail, so the force due to the solar radiation pressure is normal to its surface. The orientation of the sail is parametrised by two angles α and δ and its efficiency is given in terms of the sail lightness number β. To model the dynamics of a solar sail we have taken the Sun–Earth Restricted Three Body Problem (RTBP) and added the solar radiation pressure.

The Restricted Three Body Problem for a Solar sail (RTBPS) can be seen as a perturbation of the RTBP. If the radiation pressure is discarded ($\beta = 0$ or the sail is aligned with the Sun–sail direction) the system has five equilibrium points. If we add the solar radiation pressure and the sail is oriented perpendicular to the Sun–sail line, the system has the same qualitative behaviour as the RTBP (McInnes 2000). For this particular case, we also find 5 equilibrium points, related to the classical Lagrangian points, $L_{1,\ldots,5}$ that we call $SL_{1,\ldots,5}$. When we consider the whole set of possible sail orientations, the system has, for a fixed sail lightness number $\beta \neq 0$, a 2D families of equilibrium points parametrised by the two angles defining the orientation of the sail (α, δ) (McInnes 1999; McInnes et al. 1994).

These artificially generated equilibrium points offer the possibility of considering very interesting mission applications, two examples would be the Geostorm Warning Mission (Macdonald and McInnes 2004; Yen 2004) and the Polar Observer Mission (Macdonald and McInnes 2004). The Geostorm is a mission concept where a modest sail is placed sunwards of the classical Earth–Sun L_1 point. Then with a magnetometer we can detect the solar wind polarity and give enhanced warning of the geomagnetic storms, doubling the time of alert of a conventional L_1 Halo orbiter such as SOHO. The aim of the Polar observer mission is to place a solar sail around an equilibrium point displaced above the ecliptic plane, above one of the Earth's poles. This would provide constant viewing of the polar regions and could be useful to imaging the polar regions or carrying out studies on the climate evolution on the Arctic zone.

Both missions require to keep a solar sail close to an unstable equilibrium point. Hence we need to derive a station keeping strategy to maintain a solar sail around it. Several authors have already discussed the controllability of these regions and studied different possibilities for the station keeping of a solar sail around unstable equilibrium points (Rios-Reyes and Scheeres 2005; Lisano 2005; Bookless and McInnes 2005; Farrés and Jorba 2008a).

In Farrés and Jorba (2008a,b) we describe how to use the information of the linear dynamics close to an equilibrium point to derive station keeping strategies. The main idea is to know how the fixed points and their stable and unstable manifolds vary when the sail orientation is changed. A change on sail orientation implies a change on the phase space portrait. If we understand how these changes affect the trajectory of the sail, we can try to change the sail orientation in an appropriate way to make the phase space act in our favour. Using this idea, we can find a sequence of changes for the sail orientation, so that the trajectory of the sail remains close to the equilibrium point. The idea is to maintain the sail orientation fixed for a certain time, and when needed change its orientation. The variations on the sail orientation are small and also is the time needed to change from one orientation to the other, hence as a first approach we can consider these changes to be instantaneous. Other authors, using feedback control find a continuous change on the sail orientation that manages to maintain the sail close to the equilibrium point.

In this paper we want to study and understand the non-linear dynamics around equilibria. We want to know what other invariant objects exist in the phase space and how they change when we consider different sail orientations. In particular we will describe the families of periodic and quasi-periodic orbits. Some of these invariant objects can offer interesting possibilities for other mission applications. In the near future we want to use this information, to derive strategies in the philosophy of Farrés and Jorba (2008a,b), to maintain a solar sail close to some of THESE invariant objects.

We will focus on the particular case of $\alpha = 0$ (i.e. we just allow the sail orientation to vary vertically with respect to the Sun–sail line), when the system is time reversible. This will ensure that, under certain constraints on the nature of the equilibrium points, there exists families of periodic and quasi-periodic orbits around equilibria.

In Sect. 3 we describe the families of periodic orbits that emanate from different equilibrium points. We find planar and vertical families of periodic orbits, as well as Halo-type orbits. In Sect. 4 we describe the quasi-periodic motion around the equilibrium point, finding new families of periodic orbits and invariant tori around equilibria due to the interaction between the two frequencies defining the centre motions.

We will see that if $\alpha = \delta = 0$, i.e. the sail is perpendicular to the Sun–sail line, the qualitative behaviour of the system around the equilibrium point is similar to the behaviour around the collinear point L_1 of the RTBP. There are families of planar, vertical and Halo periodic orbits, as well as families of invariant tori. In McInnes (2000) we find a study on the behaviour of this family of Halo orbits for different values of β. We will show how the loss of symmetry of the system when $\delta \neq 0$ affects this phase space portrait.

As the equilibrium points are unstable, we need to be careful with the numerical tools that we use. We have developed our own algorithms to avoid problems during the integration due to the instability of the region. To the computation of the periodic orbits we have used a parallel shooting method. To study the quasi-periodic motion we have performed the reduction to the centre manifold. In Sect. 4.1 we give some of the main details on how to deal in an efficient way with the computation of this last invariant object.

2 Solar sails in the RTBP

To describe the motion of a solar sail in the Earth–Sun system, we take the Restricted Three Body Problem for a Solar sail (RTBPS). We assume that the Earth and Sun are point masses moving in a circular orbit around their common centre of mass, and that the sail is a massless particle that is affected by the gravitational attraction of both bodies and the solar radiation pressure. The units of mass, distance and time are normalised so that the total mass of the system is 1, the Earth–Sun distance is 1 and the period of its orbit is 2π. We use a rotation reference system so that Earth and Sun are fixed on the x-axis, z is perpendicular to the ecliptic plane and y defines an orthogonal positive oriented reference system (Fig. 1 left).

We consider the solar sail to be flat and perfectly reflecting. This means that the force due to the solar radiation pressure is in the normal direction to the surface of the sail. In such case, the force due to the sail is given by,

$$\mathbf{F}_{sail} = \beta \frac{1-\mu}{r_{PS}^2} \langle \mathbf{r}_s, \mathbf{n} \rangle^2 \mathbf{n},$$

where β represents the sail lightness number, $\mathbf{r}_s$ is the Sun–line direction and $\mathbf{n}$ is the normal direction to the surface of the sail (both vectors have norm 1). The sail orientation is parametrised by two angles, say α and δ: α is the angle between the projection of the Sun–sail

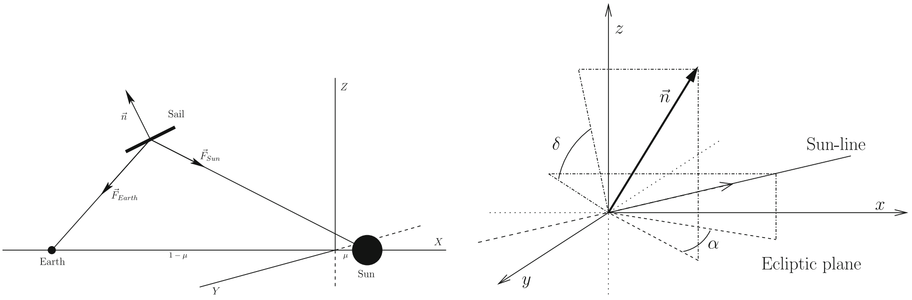

Fig. 1 *Left*: Schematic representation of the position of the two primaries and the solar sail in the synodical reference system. *Right*: Graphic description of the two angles defining the sail orientation

line and the normal vector to the surface of the sail **n** on the ecliptic plane; δ is the difference between: a) the angle between the projection of the Sun–sail line with the ecliptic plane; and b) the angle of the normal vector **n** with the ecliptic plane (see Fig. 1 right). There are other possibilities to define these angles, see (McInnes 1999; Rios-Reyes and Scheeres 2005).

The equations of motion are,

$$\begin{aligned}
\ddot{X} &= 2\dot{Y} + X - \frac{(1-\mu)}{r_{PS}^3}(X-\mu) - \frac{\mu}{r_{PE}^3}(X-\mu+1) - \beta\frac{(1-\mu)}{r_{PS}^3}\langle\mathbf{r}_s,\mathbf{n}\rangle^2 N_X,\\
\ddot{Y} &= -2\dot{X} + Y - \left(\frac{(1-\mu)}{r_{PS}^3} + \frac{\mu}{r_{PE}^3}\right)Y - \beta\frac{(1-\mu)}{r_{PS}^3}\langle\mathbf{r}_s,\mathbf{n}\rangle^2 N_Y,\\
\ddot{Z} &= -\left(\frac{(1-\mu)}{r_{PS}^3} + \frac{\mu}{r_{PE}^3}\right)Z + \beta\frac{(1-\mu)}{r_{PS}^3}\langle\mathbf{r}_s,\mathbf{n}\rangle^2 N_Z,
\end{aligned} \tag{1}$$

where, $r_{PS} = \sqrt{(X-\mu)^2+Y^2+Z^2}$, and $r_{PE} = \sqrt{(X-\mu+1)^2+Y^2+Z^2}$, are the Sun–sail and Earth-sail distances, respectively, $\mathbf{r}_s = (X-\mu, Y, Z)/r_{PS}$ is the normalised Sun–sail direction and $\mathbf{n} = (N_X, N_Y, N_Z)$ is the normal direction to the surface of the sail. Using the above definition for the sail orientation,

$$\begin{aligned}
N_X &= \frac{X-\mu}{r_{PS}}\cos\alpha\cos\delta - \frac{Z(X-\mu)}{r_{PS}r_2}\cos\alpha\sin\delta - \frac{Y}{r_{PS}}\sin\alpha\cos\delta + \frac{YZ}{r_{PS}r_2}\sin\alpha\sin\delta,\\
N_Y &= \frac{Y}{r_{PS}}\cos\alpha\cos\delta - \frac{YZ}{r_{PS}r_2}\cos\alpha\sin\delta + \frac{X-\mu}{r_{PS}}\sin\alpha\cos\delta - \frac{Z(X-\mu)}{r_{PS}r_2}\sin\alpha\sin\delta,\\
N_Z &= \frac{Z}{r_{PS}}\cos\delta + \frac{r_2}{r_{PS}}\sin\delta,
\end{aligned}$$

where $r_2 = \sqrt{(X-\mu)^2+Y^2}$. As **n** cannot point towards the Sun there are some restrictions on the normal direction, namely $\langle\mathbf{r}_s,\mathbf{n}\rangle \geq 0$. Notice that if $\beta = 0$ or $\langle\mathbf{r}_s,\mathbf{n}\rangle = 0$ the solar radiation pressure is discarded and we have the RTBP.

As we know, the RTBP can be expressed as a Hamiltonian system by introducing the momenta: $P_X = \dot{X} - Y$, $P_Y = \dot{Y} + X$, $P_Z = \dot{Z}$. Unfortunately, when we introduce the solar radiation pressure the Hamiltonian character of the system only holds for a small set of sail orientations: when the sail is aligned with the Sun–sail line (i.e. $\langle\mathbf{r}_s,\mathbf{n}\rangle = 0$ so there is no sail effect) and when the sail is perpendicular to the Sun–sail line (i.e. $\langle\mathbf{r}_s,\mathbf{n}\rangle = 1$). For the other cases, the system is not Hamiltonian, but it is still conservative (it is easy to check that, for

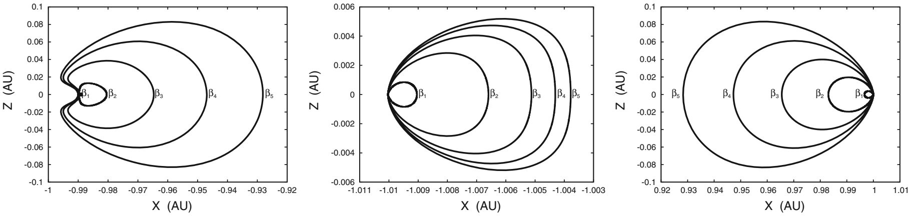

Fig. 2 Families of equilibrium points for $\beta_1 = 0.01$, $\beta_2 = 0.05$, $\beta_3 = 0.1$, $\beta_4 = 0.15$ and $\beta_5 = 0.2$. From *left* to *right*: the FL_1, FL_2 and FL_3 families of equilibria

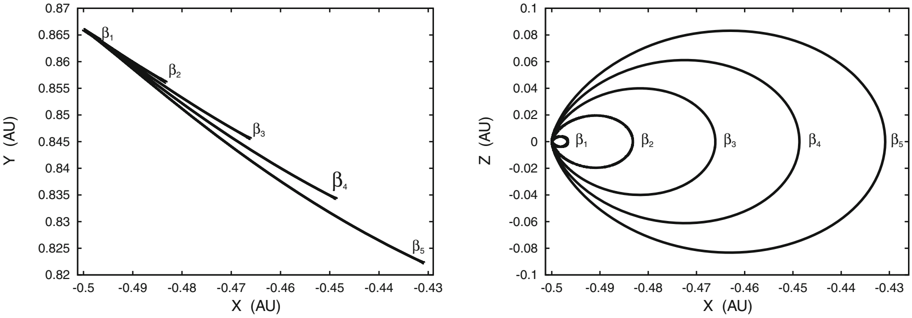

Fig. 3 FL_4 family of equilibrium points for $\beta_1 = 0.01$, $\beta_2 = 0.05$, $\beta_3 = 0.1$, $\beta_4 = 0.15$ and $\beta_5 = 0.2$. From *left* to *right*: XY projection and XZ projection

a fixed sail orientation, the divergence of the vector field is zero, hence the volume in phase space is preserved by the flow).

There is another particular case that offers interesting properties: when $\alpha = 0$ and $\delta \in [-\pi/2 : \pi/2]$. This means that we only allow vertical variations on the sail orientation with respect to the Sun–line. Here the system is time reversible by the symmetry

$$R : (X, Y, Z, \dot{X}, \dot{Y}, \dot{Z}) \rightarrow (X, -Y, Z, -\dot{X}, \dot{Y}, -\dot{Z}).$$

Hence, under certain constraints on the nature of the equilibrium points the system behaves locally as a Hamiltonian (Sevryuk 1986). In this paper we will focus on this particular case.

It is well known that the RTBP has 5 equilibrium points $L_{1,\dots,5}$ (Szebehely 1967). When the effect of the solar radiation pressure is added these 5 equilibrium points are replaced by a 2D family of equilibrium points parametrised by the two angles α and δ. If we take $\alpha = 0$ there are five 1D families of equilibria, that we call $FL_{1,\dots,5}$, parametrised by the angle δ. Each of families contains one of the classical Lagrangian equilibrium points $L_{1,\dots,5}$ and the displaced equilibrium point $SL_{1,\dots,5}$.[1] In Figs. 2 and 3 we can see these families for different values of β. Notice that as β increases these families get "larger", having fixed points higher above the ecliptic plane and closer to the Sun.

In Fig. 2 we have the families FL_1 (left), FL_2 (centre) and FL_3 (right) for different values of β, all of them are contained on the $Y = 0$ plane. For small values of β, all of these equilibrium points are unstable and their spectrum is of the form $\{\pm\lambda, \pm i\omega_1, \pm i\omega_2\}$. In Fig. 4 we show the spectrum of the fixed points for $\beta = 0.051689$. For large β the spectrum

---

[1] $SL_{1,\dots,5}$ are the equilibrium points of the system when the sail is oriented perpendicular with respect to the Sun–sail line. They are placed near the classical Lagrangian points $L_{1,\dots,5}$ but closer to the Sun (Farrés and Jorba 2009).

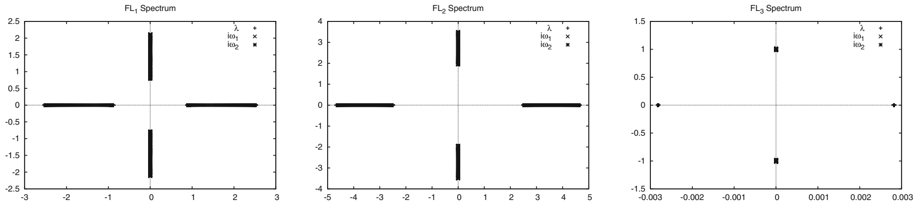

Fig. 4 Spectrum of the equilibrium points on the FL_1, FL_2 and FL_3 families for $\beta = 0.051689$

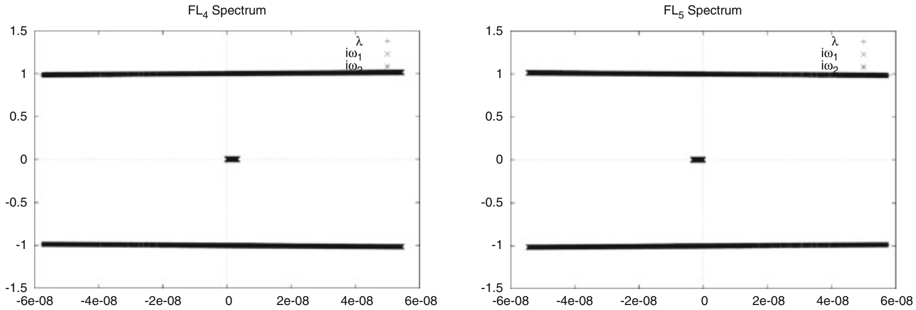

Fig. 5 Spectrum of the equilibrium points on the FL_4 and FL_5 families for $\beta = 0.051689$

of some of the equilibrium points is of the form $\{\pm\lambda_1, \pm\lambda_2, \pm \mathrm{i}\omega_1\}$ (Waters and McInnes 2007, 2008).

In Fig. 3 we have the FL_4 family for different values of β, it is no longer on the $Y = 0$ plane. The FL_5 family is symmetric to FL_4 with respect to $Y = 0$. The spectrum for all these points is $\{\gamma_1 \pm \mathrm{i}\omega_1, \gamma_2 \pm \mathrm{i}\omega_2, \gamma_3 \pm \mathrm{i}\omega_3\}$, where $\gamma_i \neq 0$ with $\gamma_1 > 0$, $\gamma_2 < 0$ and γ_3 positive on FL_4 and negative on FL_5. In Fig. 5 we see the spectrum for $\beta = 0.051689$ for FL_4 and FL_5. Notice that although $\gamma_i \neq 0$, it is very small. Hence, the equilibrium points on these two families present a very mild instability.

Our aim is to understand the dynamics of the system around different unstable equilibria of these families. We will consider the sail orientation to be fixed along time and study the dynamics for different sail orientations. In Sect. 3 we will describe the families of periodic orbits that appear around different equilibrium points. In Sect. 4 we will perform the reduction to the centre manifold around the equilibrium points and use it to describe the bounded motion around them.

In what follows we focus on the FL_1 family for $\beta = 0.051689$ and δ close to zero. The equilibrium points on the FL_1 family for δ small are placed between the Earth and the Sun close to the displaced collinear equilibrium point SL_1. We consider this region to be relevant for possible mission applications. Taking $\beta = 0.051689$ corresponds to a sail with a characteristic acceleration of $0.3\,\mathrm{mm/s^2}$ or a sail loading of $30\,\mathrm{g/m^2}$. This sail lightness number has been considered for the Geostorm Mission and is thought to be a reasonable value for a near term mission application (McInnes 1999; Macdonald and McInnes 2004; Waters and McInnes 2007). Although we only focus on a neighbourhood of equilibria of the family FL_1, the same numerical tools that we have used here can be applied to study the motion around the equilibrium points on the $FL_{2,3}$ families.

3 Periodic motion

It is well known that if we have a fixed point p_0 on a Hamiltonian system, with $\pm\mathrm{i}\omega$ as an eigenvalue, then under suitable non-resonance conditions with respect to the remaining eigenvalues λ_i, the Lyapunov Centre Theorem (Meyer and Hall 1991) ensures that there exist a one-parametric family of periodic orbits emanating from p_0, with limiting period $2\pi/\omega$. Unfortunately the Hamiltonian character of the set of equations when $\alpha = 0$ is only true for 3 values of δ ($\delta = 0$ that happens when the sail oriented perpendicular to the Sun–sail line and $\delta = \pm\pi/2$ when the sail is aligned with the Sun–sail line and there is no sail effect). As we will see in this section and the next one, the qualitative behaviour in these cases is the same.

In any case, we have already mentioned that for $\alpha = 0$ the RTBPS is time R-reversible by

$$R : (t, X, Y, Z, \dot{X}, \dot{Y}, \dot{Z}) \rightarrow (-t, X, -Y, Z, -\dot{X}, \dot{Y}, -\dot{Z}).$$

It is known (Sevryuk 1986; Lamb and Roberts 1998), that under certain constraints a time reversible system behave locally as Hamiltonian systems around an equilibrium point. In particular, around such a point the Lyapunov Centre Theorem (Devaney 1976; Moser 1958; Sevryuk 1986; Lamb and Roberts 1998) and KAM Theory (Sevryuk 1998; Lamb and Roberts 1998) also apply.

Theorem 1 (Devaney 1976) *Let $\dot{x} = f(x)$, with $f \in \mathcal{C}^2$ and $x \in \mathbb{R}^{2n}$ be an autonomous R-reversible dynamical system, where* $\dim(Fix(R)) = n$. *Let p_0 be a fixed point such that $R(p_0) = p_0$, and with $\pm\mathrm{i}\omega, \pm\lambda_2, \ldots, \pm\lambda_n$ as eigenvalues.*

Then, if $\forall\lambda_i$ we have that $\mathrm{i}\omega/\lambda_i \notin \mathbb{Z}$, there exists a one-parametric family of periodic orbits emanating from p_0, where the period of these orbits tends to $2\pi/\omega$ when approaching p_0.

This Theorem is commonly known as Devaney–Lyapunov Centre Theorem, for further details see (Devaney 1976; Sevryuk 1986).

One can check that the only equilibrium points that remain fixed by R are the ones on the FL_1, FL_2 and FL_3 families. Hence, the local behaviour around these equilibria will be Hamiltonian. Theorem 1 (Devaney 1976) assures that under non-resonant conditions between the frequencies ω_1, ω_2 we have two families of periodic orbits emanating from the fixed point.

In this section we want to describe the two families of periodic orbits that appear around an equilibrium point of the FL_1 family. We distinguish the two families by their vertical oscillation, the family related to ω_2 has a wider vertical oscillation than the one emanating from ω_1. Then, we call the *$\mathcal{P}$-Lyapunov Family* to the family of periodic orbits emanating from p_0 related to ω_1 and the *$\mathcal{V}$-Lyapunov Family* to the family emanating from p_0 related to ω_2.

Due to the symmetric reversibility properties of the system, all these families of periodic orbits are symmetric with respect to $Y = 0$. Furthermore, for δ small, the $\mathcal{P}$-Lyapunov Family cross transversally $Y = 0$ and the $\mathcal{V}$-Lyapunov Family cross transversally $Z = Z^*$ just two times. From now on, we will only consider $\delta > 0$, as the systems is also symmetric by

$$S : (X, Y, Z, \dot{X}, \dot{Y}, \dot{Z}, \delta) \rightarrow (X, Y, -Z, \dot{X}, \dot{Y}, \dot{Z}, -\delta).$$

We start taking $\delta = 0$ and studying the behaviour of the two families of periodic orbits, then we see how these families vary when $\delta \neq 0$.

To compute the families of periodic orbits, we have designed our own routines for the numerical computation and continuation of periodic orbits. For each of the families we have

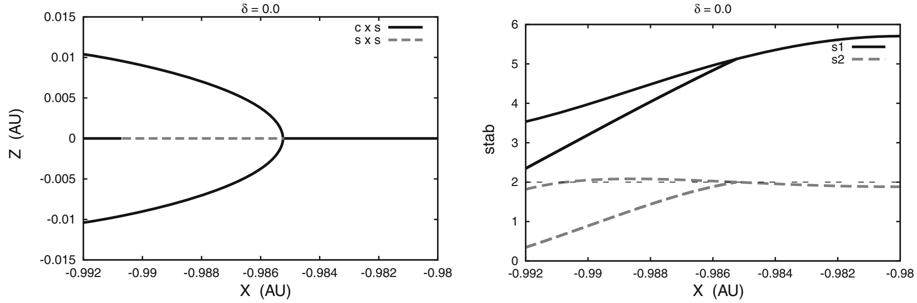

Fig. 6 $\mathcal{P}$-family of periodic orbits for $\delta = 0$. *Left*: bifurcations diagram for the continuation of periodic orbits with respect to X, continous line for centre×saddle orbits, dashed line for saddle×saddle orbits. *Right*: evolution of the stability parameters s_1 and s_2 along the family of periodic orbits

taken into account the transversality properties mentioned before. To deal with the instability of the region and to avoid difficulties in the integration of the periodic orbits we have used a multiple shooting method (Stoer and Bulirsch 2002) using two spatial sections. For the $\mathcal{P}$-Family we have taken the sections $\Gamma_1 = \{Y = 0, \dot{Y} > 0\}$ and $\Gamma_2 = \{Y = 0, \dot{Y} > 0\}$, and for the $\mathcal{V}$-Family we have taken the sections $\Sigma_1 = \{Z = Z^*, \dot{Z} > 0\}$ and $\Sigma_2 = \{Z = Z^*, \dot{Z} > 0\}$. As an initial guess for the continuation we can take the linear approximation of the solutions of the flow. We must also mention that due to the symmetries on the equations, if we take the cross section Γ_1 and Γ_2 we can save time by just integrating half of the period.

We have also computed the stability of the periodic orbits on each family. As we know, if $\phi_t(x)$ is the flow associated to an ODE, the normal behaviour around a T-periodic orbit through x_0 is given by the monodromy matrix $M = D\phi_T(x_0)$. As we are in a reversible system, the eigenvalues come in pairs, hence

$$\mathrm{spect}(M) = \{1, 1, \lambda_1, \lambda_1^{-1}, \lambda_2, \lambda_2^{-1}\}.$$

We define the *stability parameters* of the periodic orbit as $s_i = \lambda_i + \lambda_i^{-1}$ for $i = 1, 2$. We use them to describe the stability of the periodic orbit. Each s_i is related to an invariant plane by M, they can either be hyperbolic ($s_i \in \mathbb{R},\ |s_i| > 2$), elliptic ($s_i \in \mathbb{R}, |s_i| < 2$), parabolic ($s_i \in \mathbb{R},\ |s_i| = 2$) or complex unstable ($s_i \in \mathbb{C} \setminus \mathbb{R}$).

The periodic orbit has an hyperbolic direction if one of the s_i is hyperbolic and that it has an elliptic direction if one of the s_i is elliptic. Notice that if s_1 is complex unstable, then s_2 is also complex unstable, in fact $s_2 = \overline{s_1}$.

3.1 $\mathcal{P}$-family of periodic orbits

In all the computations we have considered the X coordinate of the point where the orbit crosses the section Γ_1 as the parameter of continuation.

When $\delta = 0$ the periodic orbits that are born at the equilibrium point are totally contained on the $Z = 0$ plane. In Fig. 6 we can see the continuation scheme, on the x-axis we have the continuation parameter (X) and on the y-axis the Z component of the point of the orbit on the section Γ_1. When X reaches a critical value, a pitchfork bifurcation takes place, and two new periodic orbits are born, commonly known as Halo orbits.

On the left-hand side of Fig. 6 we can see this bifurcation, the continous line corresponds to those periodic orbits with one elliptic and hyperbolic direction, and the dashed line to those

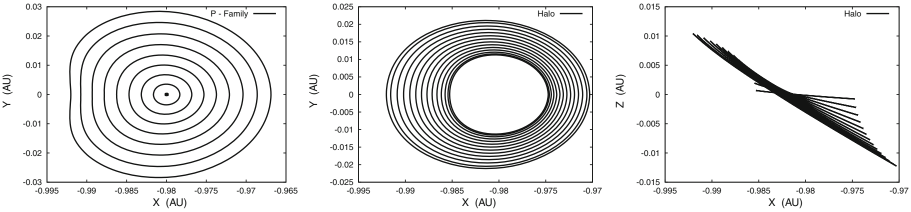

Fig. 7 XY projection on the Planar Lyapunov periodic orbits on the $\mathcal{P}$-Family (*left*). Stability parameters of the planar family of periodic orbits (*right*)

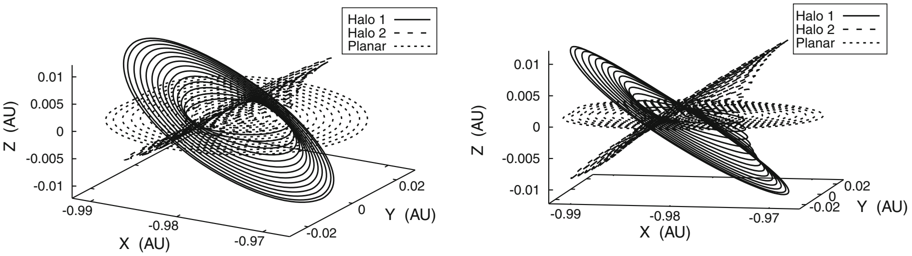

Fig. 8 Different projections on the XYZ space of the 3 different branches of periodic orbits for $\delta = 0$.

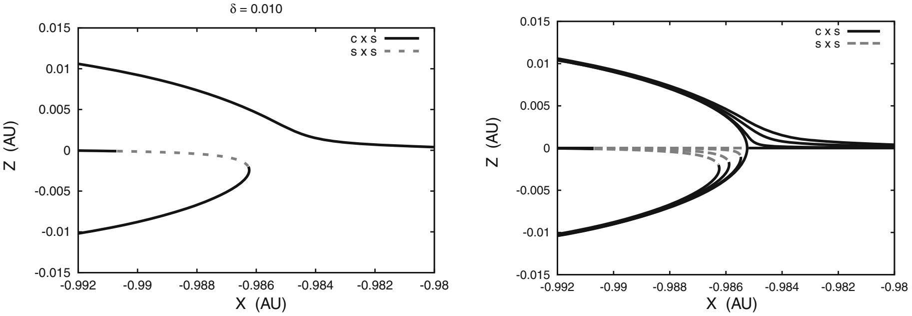

Fig. 9 Bifurcation diagram for the continuation of periodic orbits with respect to X of the $\mathcal{P}$-Family of periodic orbits for different sail orientations (δ). For $\delta = 0.001$ (*left*). Evolution of the bifurcation diagram for $\delta = 0, 0.001, 0.005, 0.01$ (*right*)

orbits with two hyperbolic directions. On the right-hand side of Fig. 6 we have the evolution on the stability parameters along the family.

On the left hand side of Fig. 7 we see the planar periodic orbits on the $\mathcal{P}$-Family, before and after the bifurcation point, this family is totally contained on the $Z = 0$ plane. In Fig. 7 (middle and right) we see different projections of one of the two families of Halo orbits. The families of Halo-type orbits for a solar sail in the RTBP when the sail is perpendicular to the Sun–sail line were found by McInnes (2000). There he studied the behaviour of these families for different values of β around SL_1 and SL_2. The other family of Halo orbits is symmetric to this one with respect to $Z = 0$. Finally, in Fig. 8 we have two different 3D projections on the position space of the three branches of the periodic orbits on the family.

When $\delta \neq 0$, as we can see in Fig. 9 there is no longer a pitchfork bifurcation giving rise to two Halo-type orbits as it happened for $\delta = 0$. Now two of the branches have split, leaving a family of periodic orbits with no change in the stability and another family with a

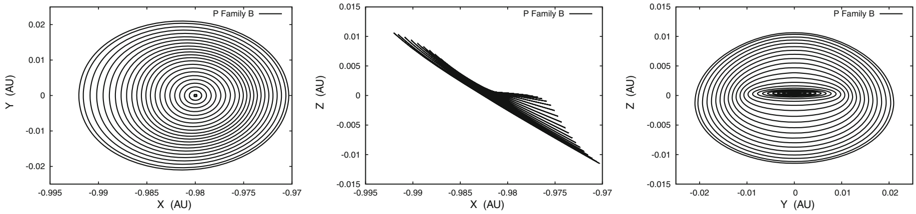

Fig. 10 For $\delta = 0.01$. Different projections of the periodic orbits on $\mathcal{P}$-Family that emanate form the fixed pint. From *left* to *right*: XY projection, XZ projection and YZ projection

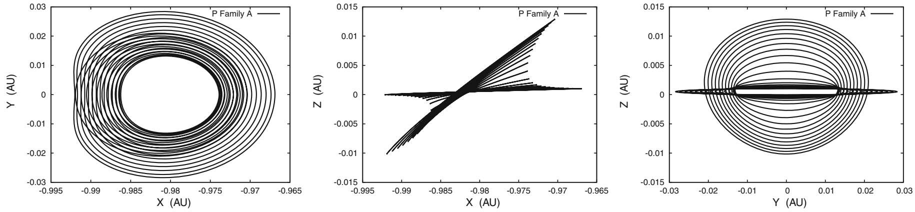

Fig. 11 For $\delta = 0.01$. Different projection of the periodic orbits on $\mathcal{P}$-Family that appear after a saddle node bifurcation. From *left* to *right*: XY projection, XZ projection and YZ projection

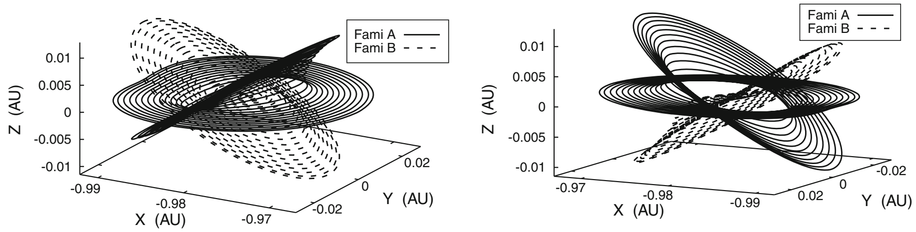

Fig. 12 Different projections on the XYZ space of the 2 disconnected branches of periodic orbits for $\delta = 0.01$

saddle-node bifurcation (Fig. 9 left). This is due to a symmetry breaking (Gulobitski et al. 1985; Crawford 1991) in the system. On the right-hand side of Fig. 9, we can see the evolution of the continuation scheme when we vary δ. Notice that the separation between the two branches increases with δ.

In Figs. 10 and 11 we can see different projections of these two families for $\delta = 0.01$. In Fig. 10 we have the family that emanates from the equilibrium point. We can see how, as the orbits amplitude increases, they gain Z amplitude ending up looking like Halo type orbits. Here all the periodic orbits have one hyperbolic and one elliptic direction. In Fig. 11 we see the family of periodic orbits that appears after the saddle-node bifurcation. The orbits on the other branch of the family that have less Z oscillation have two hyperbolic directions, while the other ones have one hyperbolic and one elliptic direction. Finally, in Fig. 12 we have different 3D projections, on the position space, of the two disconnected branches of the $\mathcal{P}$-Family of periodic orbits for $\delta = 0.01$. We can see that qualitatively behaviour for $\delta \neq 0$ is not that different to the one for $\delta = 0$, in both cases we find planar and Halo-type orbits.

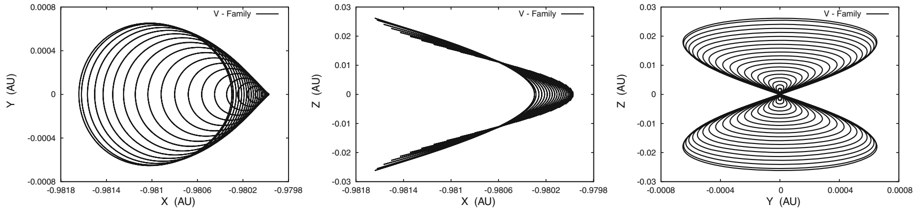

Fig. 13 For $\delta = 0$. Different projections of the periodic orbits on the $\mathcal{V}$-family. From *left* to *right*: XY projection, XZ projection and YZ projection

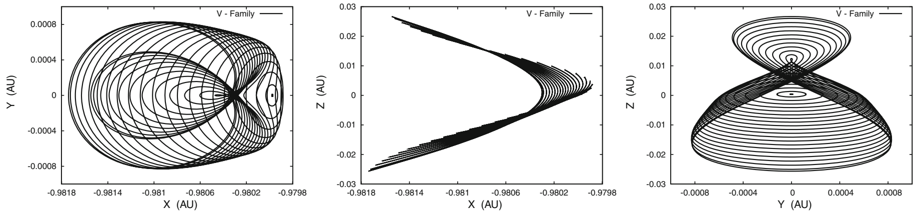

Fig. 14 For $\delta = 0.01$. Different projections of the periodic orbits on the $\mathcal{V}$-family. From *left* to *right*: XY projection, XZ projection and YZ projection

3.2 $\mathcal{V}$-family of periodic orbits

Now for all the computations we have considered the $\dot{Z}$ coordinate of the point where the orbit crosses the section Σ_1 as the parameter of continuation.

When $\delta = 0$ the periodic orbits are symmetric with respect to the planes $Z = 0$ and $Y = 0$. In Fig. 13 we have different projections of this family of periodic orbits. We can see that these orbits have a bow tie shape. All of them have one hyperbolic and one elliptic direction.

For $\delta \neq 0$ the family of periodic orbits is only symmetric with respect to the $Y = 0$ plane. Periodic orbits that are born at the equilibrium point are seen as circles on the XZ projection. As we move along the family, their shape changes and they also look like a bow tie, although it is no longer symmetric. For small δ, the shape of most of the orbits in the family is still like a bow tie. We can see that as δ increases there is more difference between the two loops on the bow tie. In Fig. 14 we have different projections of this family for $\delta = 0.01$. As before, all of these periodic orbits have one hyperbolic and one elliptic direction.

Finally, in Fig. 15 we have 3D projections on the position space of these families for different values of δ. We can see clearly how these families get more asymmetric as δ increases. In the picture we have $\delta = 0, 0.005, 0.01$ and 0.03.

4 Quasi: periodic motion

In the previous section we have described the families of periodic orbits that appear around the fixed points and studied their stability. Now we want to give a more detailed description of the non-linear dynamics around the equilibrium point.

As we know, the linear dynamics of the fixed points on the FL_1 family is the cross product of a saddle and two complex directions with zero real part and we want to

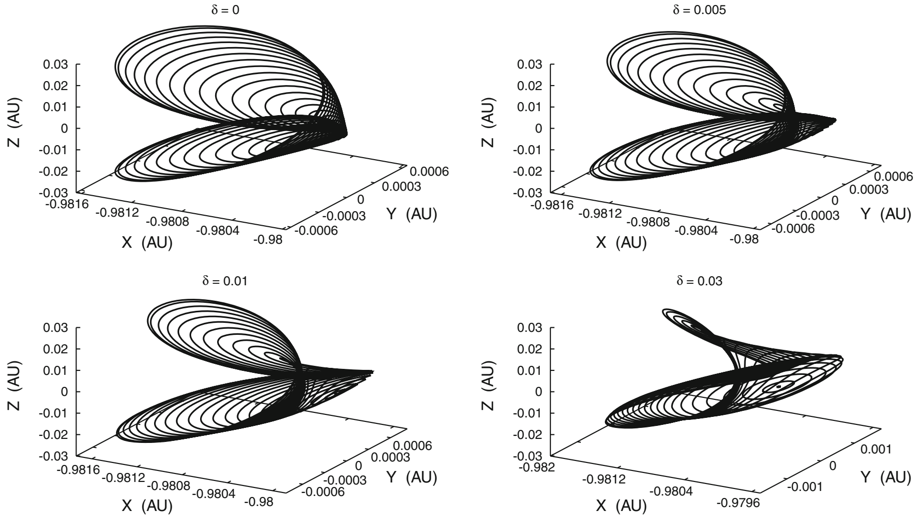

Fig. 15 Projections on the XYZ space of the $\mathcal{V}$-Family of periodic orbits for different values of δ. From *left* to *right*, *top* to *bottom*: $\delta = 0$, $\delta = 0.005$, $\delta = 0.01$ and $\delta = 0.03$

study the bounded motion around them. Due to the instability produced by the saddle, taking arbitrary initial conditions and integrating them numerically to produce plots of the orbits is not a good option as the trajectories will escape quickly. To get rid of the instability produced by the saddle, we have performed the so-called reduction to the centre manifold.

We call centre manifold to an invariant manifold that is tangent to linear subspace generated by the different pairs of complex eigenvectors that correspond to the complex eigenvalues with zero real part. We know that this invariant manifold might not be unique, although the Taylor expansion of the graph of this invariant manifold at the equilibrium point is (Carr 1981; Sijbrand 1985; Vanderbauwhede 1989). The reduction to the centre manifold process consists in finding a high order approximation of this invariant manifold and to restrict the flow to it. The main idea to compute the manifold is to uncouple the saddle direction from the other directions up to high order. Then, neglecting the reminder we obtain a high order approximation of the flow on an invariant manifold that does not contain the saddle. In this way we can do numerical integrations and study the motion around the equilibrium point on the centre manifold.

If the system is Hamiltonian we can compute this manifold using a partial normal form scheme on the Hamiltonian (Jorba 1999), but this is not the case, as the system is Hamiltonian only for a small set of parameters. To deal with this situation we have used the graph transform method (Carr 1981; Simó 1990; Farrés and Jorba 2009). The idea is to compute, formally, the power expansion of the graph of the centre manifold at the equilibrium point. In Sect. 4.1 we give the main ideas of the algorithm that we have used to compute the graph of the centre manifold $y = v(x)$ in an efficient way, for further details on the algorithm see (Farrés and Jorba 2009).

Finally, we have computed the centre manifold around several equilibrium points on the FL_1 family. For each one we have computed the Taylor series of the graph of the centre manifold up to degree 16. In Sect. 4.2 we will use this manifold to study the local dynamics around the different equilibrium point.

4.1 Reduction to the centre manifold

Let $\dot{z} = F(z)$ be an ordinary differential equation where $z \in \mathbb{R}^6$ and has a fixed point of the type centre × centre × saddle. Without loss of generality we can assume that the fixed point is at the origin. It is well known that with an appropriate linear transformation, the equations of motion can be written as:

$$\begin{aligned} \dot{x} &= Ax + f(x, y), \\ \dot{y} &= By + g(x, y), \end{aligned} \tag{2}$$

where $x \in \mathbb{R}^4$, $y \in \mathbb{R}^2$, all the eigenvalues of the matrix A have zero real part and all the eigenvalues of the matrix B are real. The functions f and g are sufficiently smooth and satisfy,

$$f(0,0) = 0, \quad D_{x,y} f(0,0) = 0, \quad g(0,0) = 0, \quad D_{x,y} g(0,0) = 0,$$

where $D_{x,y}$ denotes the first derivative with respect to (x, y). Note that $y = 0$ is the linear approximation to the centre manifold. We are interested in finding $y = v(x)$ with $v(0) = 0$ and $D_x v(0) = 0$, the local expression of the centre manifold. If we substitute this on Eqs. 2, we have that $v(x)$ must satisfy:

$$Bv(x) + g(x, v(x)) = D_x v(x)[Ax + f(x, v(x))], \tag{3}$$

and the flow restricted to the manifold is given by,

$$\dot{x} = Ax + f(x, v(x)). \tag{4}$$

To fix notation, if $x = (x_1, \ldots, x_4)$ is a vector of complex numbers and $k = (k_1, \ldots, k_4)$ a vector of integer numbers, we define $|k| = k_1 + \cdots + k_4$ and denote $x^k = x_1^{k_1} \ldots x_4^{k_4}$ (here $0^0 = 1$).

Let us assume that $\pm\lambda$, $\pm\mathrm{i}\omega_1$ and $\pm\mathrm{i}\omega_2$ are the eigenvalues of $D_z F$, and that we have performed a linear transformation such that A and B are in diagonal form. We want to find $y = v(x)$ that satisfies Eq. 3. We take $v(x) = \sum_{|k|\geq 2} v_k x^k$, with $v_k \in \mathbb{R}^2$, the power expansion of $v(x)$ around the origin and we want to find the values $v_k = (v_k^1, v_k^2)$ up to high order. This way we have a good approximation of the centre manifold, for instance, if we have $\widehat{v}(x) = \sum_{|k|=2}^{N} v_k x^k$ that satisfies Eq. 3 up to order N, then $\widehat{v}(x)$ approximates the graph of the centre manifold up to the same order, i.e. $||v(x) - \widehat{v}(x)|| = O(||x||^N)$. And $\dot{x} = Ax + f(x, \widehat{v}(x))$ is a high order approximation of the flow on the centre manifold.

Notice that Eq. 3 can be rewritten as,

$$D_x v(x) Ax - Bv(x) = g(x, v(x)) - D_x v(x) f(x, v(x)), \tag{5}$$

where the left-hand side of this equation is a linear operator with respect to $v(x)$ and the right-hand side a non-linear one. As A and B are in diagonal form, then the left-hand side of Eq. 5 takes the diagonal form,

$$D_x v(x) Ax - Bv(x) = \begin{pmatrix} \displaystyle\sum_{|k|\geq 2} (\mathrm{i}\omega_1 k_1 - \mathrm{i}\omega_1 k_2 + \mathrm{i}\omega_2 k_3 - \mathrm{i}\omega_2 k_4 - \lambda)\, v_k^1\, x^k \\ \\ \displaystyle\sum_{|k|\geq 2} (\mathrm{i}\omega_1 k_1 - \mathrm{i}\omega_1 k_2 + \mathrm{i}\omega_2 k_3 - \mathrm{i}\omega_2 k_4 + \lambda)\, v_k^2\, x^k \end{pmatrix}. \tag{6}$$

Let $h(x) = g(x, v(x)) - D_x v(x) f(x, v(x))$ be the right hand side of Eq. 5. We take its expansion $h(x) = \sum_{|k|\geq 2} h_k x^k$ around the origin ($h_k = (h_k^1, h_k^2)$), where the coefficients

h_k depend on the coefficient of v_k in a known way. It can be seen that the coefficients h_k for $|k| = n$ depend on v_k with $|k| < n$ (see Farrés and Jorba 2009). Hence, we can find the coefficients v_k up to degree N in an iterative way. We already know that $v_k = 0$ for $|k| = 0, 1$, as $v(0) = 0$ and $D_x v(0) = 0$. Then we can compute v_k for $|k| = 2, \ldots, N$ by solving at each step the diagonal linear system in Eq. 5.

This process is carried out up to a sufficiently high order N. Finally, we have the expansion up to degree N of the local central manifold,

$$\widehat{v}(x) = \sum_{|k|\geq 2}^{N} v_k x^k.$$

Once this is done, we are ready to explore the phase space. We will use $\dot{x} = Ax + f(x, \widehat{v}(x))$ to integrate the flow and have a good description of the motion on the centre manifold.

Remark 1 To have an efficient algorithm, we need to find an efficient way to compute the coefficients h_k. As we know they come from the expansion around the origin of

$$h(x) = g(x, v(x)) - D_x v(x) f(x, v(x)).$$

Expanding $g(x, y)$ and $f(x, y)$ and then composing with $v(x)$ is NOT a good option, as it is very hard in terms of computational time. To obtain a more efficient algorithm we propose to find a recurrent expressions for the expansion of the non-linear terms and use these expressions to compute the composition of these functions with $v(x)$. For more details on how to use these recurrent expression see (Farrés and Jorba 2009).

Remark 2 It is not necessary to have A and B in their diagonal form, but then the linear part of Eq. 5 will not take a diagonal form. Then, as we increase the degree, the dimension of the linear system we have to solve increases and so does the computational cost and error propagation while solving it.

The linear system can be solved if and only if

$$\mathtt{i}\omega_1(k_1 - k_2) + \mathtt{i}\omega_2(k_3 - k_4) \mp \lambda \neq 0.$$

This is always true as $\lambda \in \mathbb{R} \setminus \{0\}$ and $\mathtt{i}\omega_1$, $\mathtt{i}\omega_2$ are pure imaginary numbers.

4.2 Dynamics on the centre manifold

Using the algorithm explained before we have computed the centre manifold around several equilibrium points of the FL_1 family (i.e. different sail orientations). For each one we have computed the Taylor series up to degree 16 of the graph of the centre manifold, $y = v(x)$. Using an Intel Xeon CPU at 3.40 GHz this takes around 22 s of CPU time.

Once we have reduced to the centre manifold, we are on a 4D phase space. Let (x_1, x_2, x_3, x_4) be the local coordinates on the centre manifold. A 4D phase space is difficult to visualise, so we need to perform suitable Poincaré sections to reduce the phase space dimension.

4.2.1 When the sail is perpendicular

As we have already said, when $\delta = 0$, the system is still Hamiltonian. We take advantage of this to help us visualise the phase space. As we know, the Jacobi constant

$$J_C = (\dot{X}^2 + \dot{Y}^2 + \dot{Z}^2) - 2\widehat{\Omega}(X, Y, Z),$$

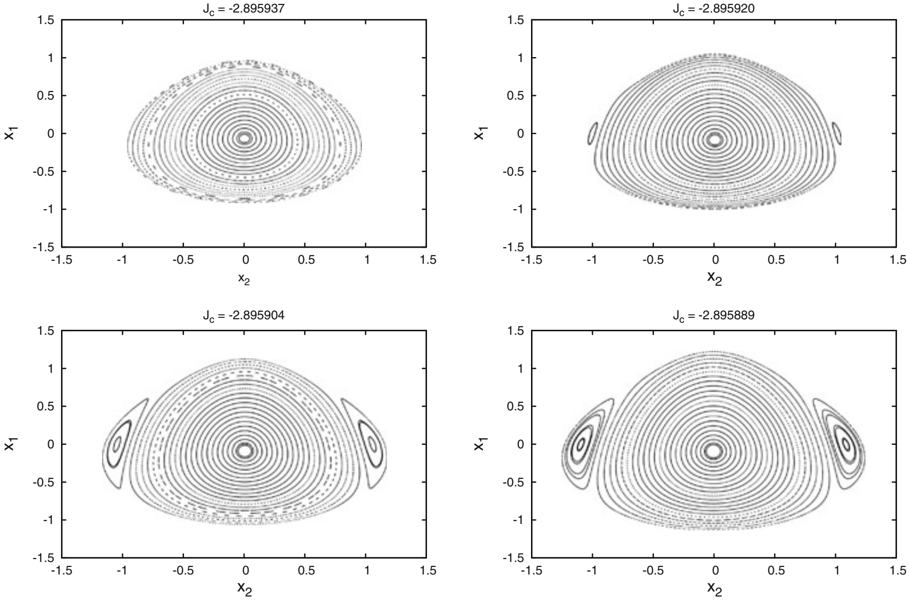

Fig. 16 For $\delta = 0$; Poincaré section $x3 = 0$ for different energy levels. From *left* to *right*, *top* to *bottom* $J_C = -2.895937, -2.895920, -2.895904, -2.895889$

with the modified potential $\widehat{\Omega}(X, Y, Z) = \frac{1}{2}(X^2 + Y^2) + \frac{(1-\mu)(1-\beta)}{r_{PS}} + \frac{\mu}{r_{PE}}$, is a first integral of the system. Hence it remains constant along time for a given trajectory. We group the trajectories on the phase space by the value of the Jacobi constant (J_C).

To visualise the dynamics on the centre manifold, we first take the Poincaré section $x_3 = 0$ and fix J_C to determine x_4. One can check that taking $x_3 = 0$ is the same as to take $z = 0$ and that x_4 is related to $\dot{z}$. Hence, x_1, x_2 are a linear transformation of the $\{x, y\}$-plane. For each J_C we take several initial conditions and compute 500 iterates on the Poincaré sections. Figure 16 shows the results for $J_C = -2.895937, -2.895920, -2.895904$ and -2.895889. We can see that for a fixed J_C, the motion on the section is bounded by the Planar Lyapunov orbit, which is fully contained on this section. The Vertical Lyapunov orbit is the central fixed point, as it crosses transversally this section close to the origin.

For small values of J_C, the coupling of the two frequencies, ω_1 and ω_2, gives rise to a family of invariant tori. As J_C varies, the Planar Lyapunov orbit changes its stability and the well know Halo orbits appear (see Sect. 3.1). These orbits correspond to the two new fixed points on the section, as the Halo orbits also cross transversally this section. We still see families of invariant tori around the fixed points and around the two Halo orbits.

Notice that $x_3 = 0$ is not the only Poincaré section that we can do. We chose this one for classical reasons, and because we know that $Z = 0$ is a cross section and the motion is symmetric with respect to this plane. But we could chose another one, for instance $Y = 0$ is also a cross section and a symmetry plane.

Now taking $x_2 = 0$ is similar to taking $Y = 0$. Then we determine x_1 from the J_C, that is similar to taking $\dot{Y}$. Now we repeat the same process as before, take a value for J_C and several initial conditions x_3, x_4 and compute 500 Poincaré sections for each one. Figure 17 shows the results for the same energy levels as before.

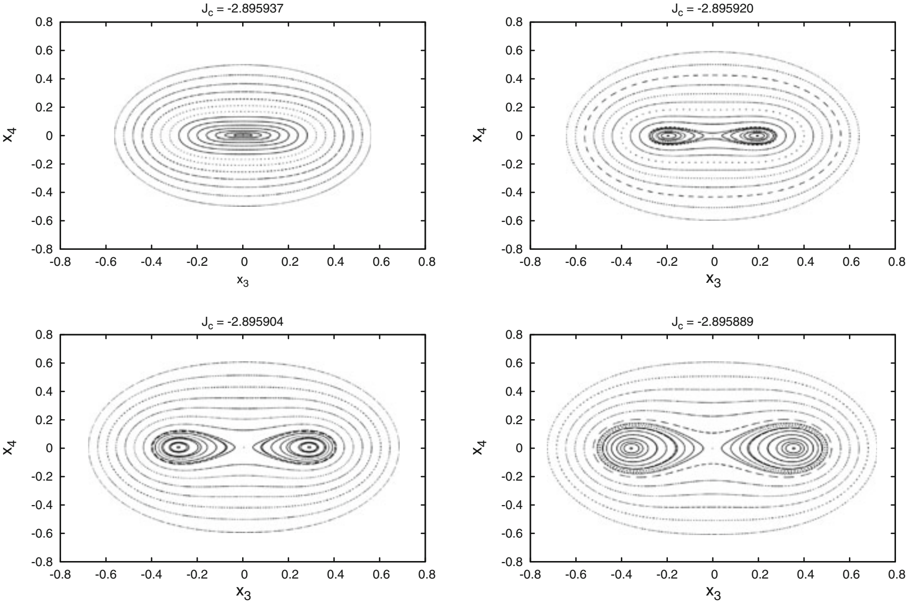

Fig. 17 For $\delta = 0$; Poincaré section for $x_2 = 0$ for different energy levels. From *left* to *right*, *top* to *bottom* $J_C = -2.895937, -2.895920, -2.895904, -2.895889$

Now the Planar Lyapunov orbit is the central fixed point. As before, we can see that for small values of the energies, we have a family of invariant tori due to the coupling of the two frequencies. As the energy level increases the Planar Lyapunov orbit changes its stability and the two Halo orbits appear. Here we can clearly appreciate the pitchfork bifurcation of the Planar Lyapunov orbit that gives rise to the Halo orbits that was mentioned in Sect. 3.

We note that the behaviour here is qualitatively the same as for the RTBP close to the collinear points. Now we want to see how this varies when the sail is no longer perpendicular to the Sun–line (i.e. when $\delta \neq 0$).

4.2.2 *When the sail is not perpendicular*

Now we take different values for the sail orientation $\delta_1 = 0.005$ and $\delta_2 = 0.01$ and do the same analysis. The main difference is that now the system is not Hamiltonian, hence we do not have a first integral to help us reduce the phase space dimension. Nevertheless, we use the quantity:

$$\widetilde{J}_C = (\dot{X}^2 + \dot{Y}^2 + \dot{Z}^2) - 2\widehat{\Omega}(X, Y, Z) + 2\beta(1-\mu)\frac{Zr_2}{r_{PS}^3}\cos^2\delta\sin^2\delta.$$

Notice that for $\delta = 0$, $\widetilde{J}_C$ is the Jacobi constant that we have used before. This value varies little along the trajectories, we will use it as an "approximated energy level" and will help us to compare the Hamiltonian behaviour with this non-Hamiltonian one.

When the system is Hamiltonian and we take several initial conditions with the same energy level, their trajectories are in the same surface of fixed energy. Hence, we are reducing in one the phase space dimension. When the system is not Hamiltonian and we take several initial conditions with the same $\widetilde{J}_C$, the "approximated energy level", the value $\widetilde{J}_C$

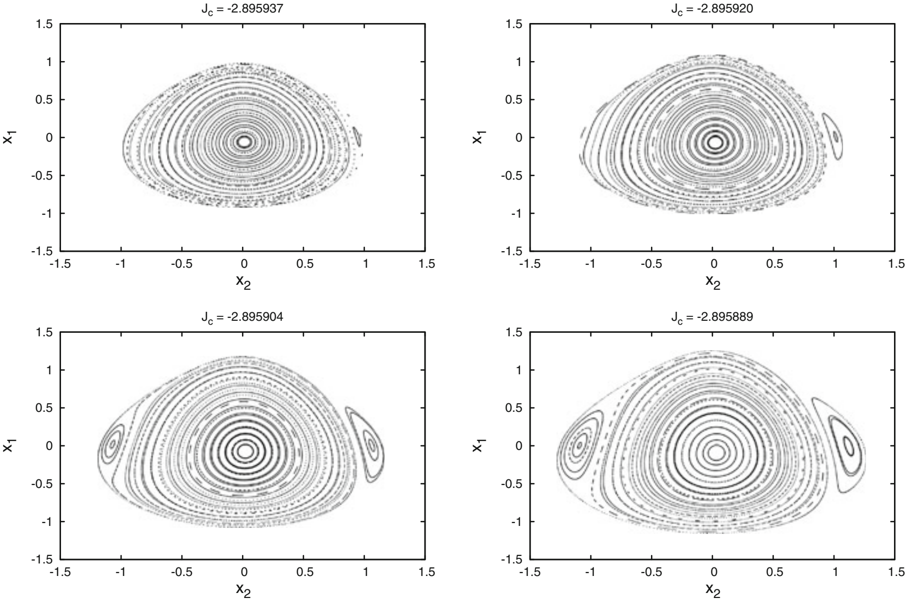

Fig. 18 For $\delta = 0.005$; Poincaré section for $x_3 = 0$ for different $\widehat{J}_C$. From *left* to *right*, *top* to *bottom* $\widetilde{J}_C = -2.895937, -2.895920, -2.895904, -2.895889$

does not remain fixed for all of the points on the trajectories. But it can be seen that close to the equilibrium point, $\widetilde{J}_C$ varies slightly. We can say that the orbits are on a thin neighbourhood of the surface $\widetilde{J}_C = constant$. Then, the projection of the trajectories on a fixed surface of fixed $\widetilde{J}_C$ should be good enough.

As before we first perform the Poincaré section $x_3 = 0$. Now this is like taking the cross section $Z = Z^*$. We use the $\widetilde{J}_C$ to determine x_4, that is related to $\dot{Z}$. We now take different initial conditions (x_1, x_2) and perform 500 iterates on the Poincaré section for different $\widetilde{J}_C$. Figures 18 and 19 show, for $\delta = 0.005$ and $\delta = 0.01$, respectively, these Poincaré sections for $\widetilde{J}_C = -2.895937, -2.895920, -2.895904$ and -2.895889. As before, we see that for small energy levels the coupling between the two frequencies gives rise to families of invariant tori around the equilibrium point. Now the central fixed point corresponds to the Vertical Lyapunov periodic orbit, that crosses transversally this section, and the Planar Lyapunov orbit bounds the motion on the section. As $\widetilde{J}_C$ varies, one Halo orbit appears, seen as the fixed point that appears on the right hand side of the Poincaré sections. If we remember the behaviour of the $\mathcal{P}$-Family of periodic orbits for $\delta \neq 0$ in Sect. 3.1, this family starts with a small $\dot{Z}$ amplitude. There is a point close to the saddle node bifurcation where the $\dot{Z}$ amplitude starts to grow significantly, having Halo-type type orbit. When the orbit gains Z amplitude, it is transversal to this Poincaré section, and we see it appear as a new fixed point. When the saddle-node bifurcation takes place, another Halo-type orbit appear, as can be seen in Figs. 18 and 19. We can see that the two Halo orbits are no longer symmetric to each other, as well as the behaviour around them.

Now we take the Poincaré section $x_2 = 0$, which is at first order equivalent to $Y = 0$, and we fix $\widetilde{J}_C$ to determine x_1. As before we take several initial conditions (x_3, x_4) and perform 500 iterates on the Poincaré section for different $\widetilde{J}_C$. Figures. 20 and 21 show, for $\delta = 0.005$ and $\delta = 0.01$, respectively, the Poincaré section $x_2 = 0$ for different values for $\widetilde{J}_C$.

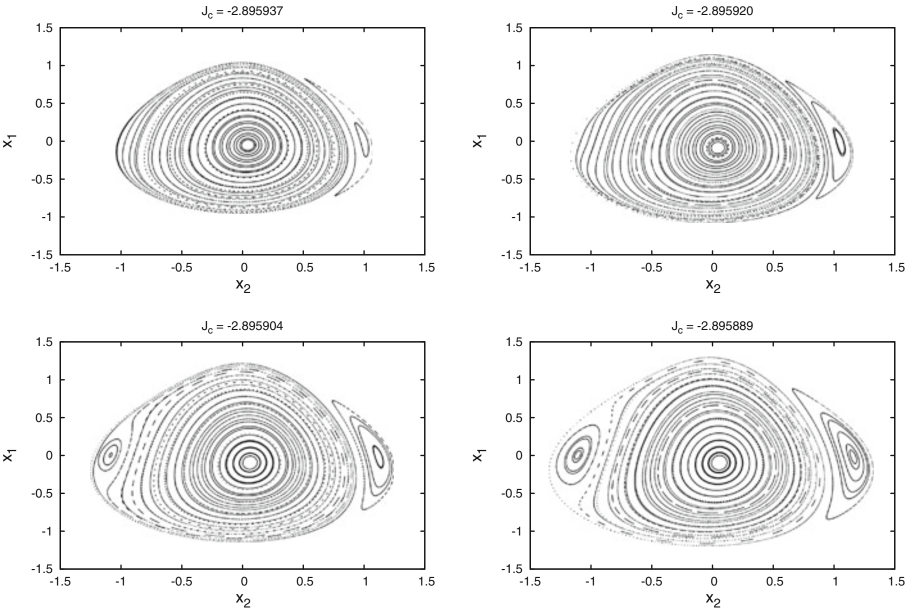

Fig. 19 For $\delta = 0.01$; Poincaré sections for $x_3 = 0$ for different $\widehat{J_C}$. From *left* to *right*, *top* to *bottom* $\widetilde{J_C} = -2.895937, -2.895920, -2.895904, -2.895889$

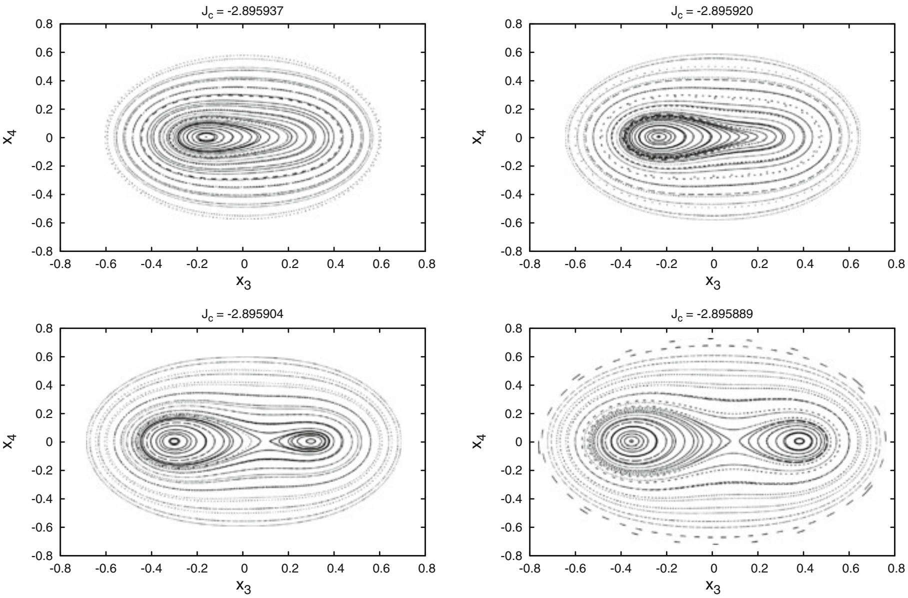

Fig. 20 For $\delta = 0.005$; Poincaré sections for $x_2 = 0$ for different $\widehat{J_C}$. From *left* to *right*, *top* to *bottom* $\widetilde{J_C} = -2.895937, -2.895920, -2.895904, -2.895889$

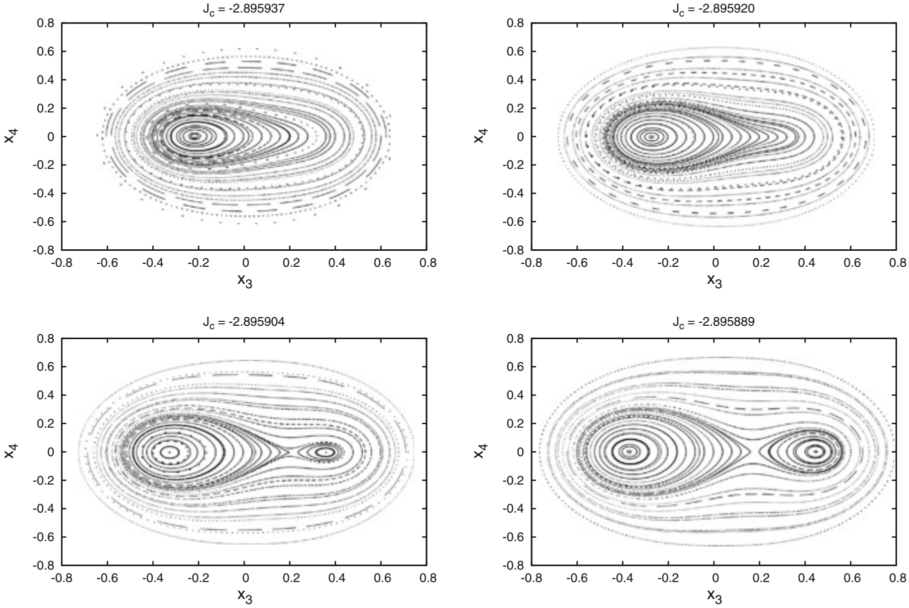

Fig. 21 For $\delta = 0.01$; Poincaré sections for $x_2 = 0$ for different $\widehat{J}_C$. From *left* to *right*, *top* to *bottom* $\widetilde{J}_C = -2.895937, -2.895920, -2.895904, -2.895889$

Now the fixed point in the centre corresponds to an orbit of the $\mathcal{P}$-Family. For small values of $\widetilde{J}_C$ we just see the families of invariant tori around the fixed point. As this energy increases, we can see how the fixed point, i.e. Planar Lyapunov Orbit, shifts to the left, and two new periodic orbits appear, one stable and one unstable, giving rise to the new Halo-type orbit. Here we can clearly appreciate the saddle-node bifurcation on the family of periodic orbits that was seen in Sect. 3.1.

If we remember Fig. 17, we saw that the planar family of periodic orbits experiences a pitchfork bifurcation as the energy level increases, which gives rise to the Halo orbits. Now in Figs. 20 and 21 we can see how for $\delta \neq 0$, due to the symmetry breaking on the equations motion, this bifurcation is replaced by a saddle-node bifurcation.

The main different between the behaviour for $\delta = 0.005$ or $\delta = 0.01$ is that the phase space is less symmetric as δ increases.

5 Conclusion

In this paper we have focused on the understanding of the non-linear dynamics for different equilibrium points close to the displaced collinear point SL_1. We have restricted to the particular case $\alpha = 0$ to take advantage of the reversible character of the system, as it ensures the existence of families of periodic orbits and invariant tori.

For this study we have computed the families of periodic orbits by means of a continuation method. Furthermore, we have performed the reduction to the centre manifold using the graph transform method around the different equilibrium points to have a better understanding of the bounded motion.

We find that when the sail is perpendicular to the Sun–line the system behaves qualitatively as the RTBP. The two frequencies defining the centre motion give rise to two families of periodic orbits, a planar and a vertical family, and we find families of invariant tori due to the coupling of the two frequencies. As we move along the planar family of periodic orbits a pitchfork bifurcation takes place, and two families of Halo-type orbits appear.

When the sail is no longer perpendicular to the Sun–line ($\delta \neq 0$) this behaviour varies slightly. We still have two families of periodic orbits emanating from the two fixed points, each one related to one of the two frequencies defining the centre motion. We no longer have a pitchfork bifurcation that gives rise to the Halo-type orbits, this one has been replaced by a saddle-node bifurcation due to the symmetry breaking of the system. Finally, we also find families of invariant tori due to the interaction between the two frequencies.

The applicability of these new families of periodic orbits is yet to be discussed. But for instance, a mission in the philosophy of "Geostorm" could be considered, where the sail would orbit around a Halo orbit for a solar sail perpendicular to the Sun–sail line. These orbits are closer to the Sun than a Halo orbit of the RTBP and would also allow early enhanced warning of the Sun's geomagnetic storms. A study on the controllability of these orbits and a comparison on the advantages of maintaining a sail around these orbits should be done to make further conclusions. Another interesting application, would be to consider a periodic orbit high above the ecliptic plane, with the same period as the Earth's rotation axis. With such an orbit it would be able to track a certain region of the Earth's pole (Waters and McInnes 2007).

Finally, let us mention that in a real application one should also consider other effects (planets, variations in the solar radiation pressure, etc), including errors in the position and orientation of the sail (for instance, α cannot be exactly zero as needed for the orbits in this paper). This, jointly with the natural instability of these orbits, implies the use of a station keeping strategy.

Acknowledgments This work has been supported by the MEC grant MTM2009-09723 and the CIRIT grant 2009 SGR 67.

References

Bookless, J., McInnes, C.R.: Control of Lagrange point orbits using solar sail propulsion. In: Proceedings of the 56th International Astronautical Congress (2005)

Carr, J.: Applications of Centre Manifold Theory. Springer, New York (1981)

Crawford, J.D.: Introduction to bifurcation theory. Rev. Modern Phys. **64**, 991–1037 (1991)

Devaney, R.L.: Reversible diffeomorphisms and flows. Trans. Am. Math. Soc. **218**, 89–113 (1976)

Farrés, A., Jorba, À.: Dynamical system approach for the station keeping of a solar sail. J. Astronaut. Sci. **58**, 199–230 (2008a)

Farrés, A., Jorba, À.: Solar sail surfing along families of equilibrium points. Acta Atronaut. **63**, 249–257 (2008b)

Farrés, A., Jorba, À.: On the high order approximation of the centre manifold for ODEs. preprint (2009)

Gulobitski, M., Schaeffer, D.G., Stewart, I.N.: Singularities and Groups in Bifurcation Theory. Springer, New York (1985)

Jorba, À.: A methodology for the numerical computation of normal forms, centre manifolds and first integrals of Hamiltonian systems. Exp. Math. **8**, 155–195 (1999)

Lamb, J.S.W., Roberts, J.A.G.: Time-reversal symmetry in dynamical systems: a survey. Phys. D Nonlinear Phenom. **112**, 1–39 (1998)

Lisano, M.: Solar sail transfer trajectory design and station keeping control for missions to Sub-L1 equilibrium region. In: Proceedings of the 15th AAS/AIAA Space Flight Mechanics Conference. Colorado (2005)

Macdonald, M., McInnes, C.R.: A near-term road map for solar sailing. In: Proceedings of the 55th International Astronautical Congress, Vancouver (2004)

McInnes, A.: Strategies for Solar Sail Mission Design in the Circular Restricted Three-Body Problem, Master Thesis. Purdue University (2000)
McInnes, C.R.: Solar Sailing: Technology, Dynamics and Mission Applications. Springer-Praxis, London (1999)
McInnes, C.R., McDonald, A.J.C., Simmons, J.F.L., MacDonald, E.W.: Solar sail parking in restricted three-body system. J. Guid. Control Dyn. **17**, 399–406 (1994)
Meyer, K.R., Hall, G.R.: Introduction to Hamiltonian Dynamical Systems and the N-Body Problem. Springer, New York (1991)
Moser, J.K.: On the generalization of a theorem of A. Liapounoff. Comm. Pure Appl. Math. **11**, 257–271 (1958)
Rios-Reyes, L., Scheeres, D.J.: Robust solar sail trajectory control for large pre-launch modelling errors. In: Proceedings of the AIAA Guidance, Navigation and Control Conference (2005)
Sevryuk, M.B.: Reversible Systems. Springer, Berlin (1986)
Sevryuk, M.B.: The finite-dimensional reversible KAM theory. Physica D Nonlinear Phenomena **112**, 132–147 (1998)
Sijbrand, J.: Properties of the centre manifold. Trans. Am. Math. Soc. **289**, 431–469 (1985)
Simó, C.: Analytical and numerical approximation of invariant manifolds. In: Froeschlé, C., Benest, D. (eds.) Les méthodes modernes de la Mecánique Céleste, pp. 285–329. Editions Frontières, Gif-sur-Yvette (1990)
Stoer, J., Bulirsch, B.: Introduction to Numerical Analysis. Springer, New York (2002)
Szebehely, V.: Theory of Orbits: The Restricted Problem of Three Bodies. Academic Press, New York (1967)
Vanderbauwhede, A.: Centre manifolds, normal forms and elementary bifurcations. In: Dynamics Reported. A Series in Dynamical Systems and their Applications, vol. 2 , John Wiley & Sons Ltd (1989)
Waters, T.J., McInnes, C.R.: Periodic orbits above the ecliptic plane in the solar sail restricted 3-body problem. J. Guid. Control Dyn. **30**, 786–793 (2007)
Waters, T.J., McInnes, C.R.: Invariant manifolds and orbit control in the solar sail 3-body problem. J. Guid. Control Dyn. **31**, 554–562 (2008)
Yen, C.W.: Solar sail geostorm warning mission design. In: Proceedings of the 14th AAS/AIAA Space Flight Mechanics Conference. Hawaii (2004)